

Assimilation of water vapor sensitive infrared brightness temperature observations during a high impact weather event

Jason A. Otkin¹

Received 2 February 2012; revised 16 August 2012; accepted 3 September 2012; published 4 October 2012.

[1] A regional-scale Observing System Simulation Experiment was used to examine the impact of water vapor (WV) sensitive infrared brightness temperature observations on the analysis and forecast accuracy during a high impact weather event across the central U.S. Ensemble data assimilation experiments were performed using the ensemble Kalman filter algorithm in the Data Assimilation Research Testbed system. Vertical error profiles at the end of the assimilation period showed that the wind and temperature fields were most accurate when observations sensitive to WV in the upper troposphere were assimilated; however, the largest improvements in the cloud and moisture analyses occurred after assimilating observations sensitive to WV in the lower and middle troposphere. The more accurate analyses at the end of these cases lead to improved short-range precipitation forecasts compared to the Control case in which only conventional observations were assimilated. Equitable threat scores were consistently higher for all precipitation thresholds during the WV band forecasts. These results demonstrate that the ability of WV-sensitive infrared brightness temperatures to improve not only the 3D moisture distribution, but also the temperature, cloud, and wind fields, enhances their utility within a data assimilation system.

Citation: Otkin, J. A. (2012), Assimilation of water vapor sensitive infrared brightness temperature observations during a high impact weather event, *J. Geophys. Res.*, *117*, D19203, doi:10.1029/2012JD017568.

1. Introduction

[2] Atmospheric water vapor (WV) is a critical component of the hydrological cycle and exerts a strong influence on sensible weather through its effect on cloud cover and precipitation processes. Small changes in the spatial distribution of WV can have a profound impact on the generation and subsequent evolution of high-impact weather events, such as severe thunderstorms, winter storms, heavy rainfall, and tropical cyclones. For instance, dry air in the lower troposphere during the winter often delays the onset of surface precipitation associated with extratropical cyclones and can lead to challenging snowfall forecasts due to the potential impact of evaporative cooling on precipitation type. Prior studies [e.g., *Sanders and Gyakum*, 1980] have also shown that latent heat release induced by a burst of heavy precipitation can lead to a period of very rapid cyclogenesis and the development of hazardous weather conditions. Excessive rainfall can occur in the presence of abundant moisture (hereafter, used interchangeably with “WV”) and persistent moisture convergence. For thunderstorms, the magnitude of

the convective available potential energy that a storm can access is determined by the vertical distribution of WV and temperature. Dry air in the middle troposphere associated with an elevated mixed layer often prevents the initiation of widespread deep convection, yet its presence can lead to more destructive thunderstorms if the capping inversion can be eliminated [e.g., *Carlson et al.*, 1983]. The WV distribution also plays an important role during the development of tropical cyclones by modulating the amount and location of latent heat release [*Palmen*, 1948; *Riehl*, 1948; *McBride and Zehr*, 1981].

[3] Accurate forecasts of cloud cover, surface precipitation, and storm evolution are more likely to occur when the spatial distribution of WV is accurately specified in the initialization data sets used by numerical weather prediction models. Unfortunately, WV is highly variable in both space and time and is poorly sampled by in situ observations. Radiosonde humidity profiles are very valuable, but typically are available only twice per day, are unevenly distributed, and have limited accuracy in the upper troposphere [*Miloshevich et al.*, 2006]. Surface observations are available more often, but do not provide any direct information about the vertical structure of the WV distribution. The scarcity of conventional WV observations, particularly over the oceans, enhances the value of remotely sensed satellite observations that are sensitive to WV, such as those from infrared and microwave sensors. Thermal infrared imagers and sounders onboard geosynchronous satellites, such as the Geostationary Operational Environmental Satellites (GOES), are especially useful because of their high spatial and

¹Cooperative Institute for Meteorological Satellite Studies, University of Wisconsin-Madison, Madison, Wisconsin, USA.

Corresponding author: J. A. Otkin, Cooperative Institute for Meteorological Satellite Studies, University of Wisconsin-Madison, 1225 W. Dayton St., Madison, WI 53706, USA. (jason.otkin@ssec.wisc.edu)

This paper is not subject to U.S. copyright.
Published in 2012 by the American Geophysical Union.

temporal resolution and large coverage area. A comprehensive study of the global impact of the primary humidity observing systems by *Andersson et al.* [2007] found that WV observations have a significant impact on the accuracy of forecasts generated by the European Centre for Medium-Range Weather Forecasts model. Radiosonde and surface station observations were dominant over land, whereas microwave sensors had their greatest impact over the oceans and infrared sounders were most important in the upper troposphere. The efficient use of satellite WV observations in modern data assimilation systems whether as radiances or WV profile retrievals has the potential to greatly reduce uncertainties in the initial WV distribution that adversely affect model forecast accuracy [*Fabry and Sun*, 2010].

[4] Early studies obtained useful information about the moisture field from infrared observations by generating derived quantities, such as vertical profiles of latent heating, dew point depression, and cloud liquid water, that were based on diagnosed cloud types [*Krishnamurti et al.*, 1984; *Donner*, 1988; *Puri and Miller*, 1990; *Puri and Davidson*, 1992; *Wu et al.*, 1995]. These data were especially useful for limiting the time required by a model to spin-up realistic cloud features after its initialization. Subsequent work by *Schmit et al.* [2002] and *Zapotocny et al.* [2005] found that directly assimilating three-layer precipitable water (PWAT) retrievals from the GOES sounder over land improved Eta model humidity and precipitation forecasts for up to 48 h. These studies also showed that the higher temporal resolution of the GOES observations provided a larger forecast impact than was achieved using observations from polar orbiting sensors. *Raymond et al.* [2004] used a suboptimal assimilation approach to extract information from the WV band brightness temperatures on the GOES imager. Even with their simple approach, modest improvements were made to the upper level moisture field.

[5] Recent studies have used advanced assimilation methods to directly assimilate WV sensitive infrared radiances and WV profile retrievals. *Li and Liu* [2009] and *Liu et al.* [2011] found that WV and temperature retrievals from the Advanced Infrared Sounder (AIRS) and the Moderate-resolution Imaging Spectroradiometer (MODIS) reduced hurricane forecast intensity and track errors when assimilated using an ensemble Kalman filter (EnKF) [*Evensen*, 1994] assimilation system. Hurricane forecasts were also improved when AIRS WV retrievals were assimilated using a 3DVAR assimilation system [*Pu and Zhang*, 2010]. Precipitation forecasts for an extremely heavy rainfall event were more accurate when AIRS WV profiles were assimilated [*Singh et al.*, 2008]. Direct radiance assimilation using both 3DVAR and 4DVAR systems has also been shown to improve the analysis and forecast accuracy [*Köpken et al.*, 2004; *Munro et al.*, 2004; *Stengel et al.*, 2010; *Singh et al.*, 2010, 2011].

[6] In this study, a regional-scale Observing System Simulation Experiment (OSSE) is used to evaluate the impact of WV-sensitive infrared brightness temperatures from the Advanced Baseline Imager (ABI) on the analysis and forecast accuracy during a high-impact weather event. The ABI is a 16-band imager that will be launched onboard the GOES-R geosynchronous satellite in 2016 [*Schmit et al.*, 2005]. Accurate radiance and reflectance measurements with high spatial and temporal resolution will provide detailed

information about surface temperatures and the tropospheric WV and cloud distributions over a large geographic domain. The paper is organized as follows. The ensemble data assimilation system and the methodology used to generate the simulated observations are described in Section 2. A brief overview of the meteorological conditions during the case study is given in Section 3. Analysis and forecast results are shown in Sections 4 and 5, with conclusions presented in Section 6.

2. Experimental Design

2.1. Forecast Model

[7] Version 3.3 of the Weather Research and Forecasting (WRF) numerical weather prediction model was used during this study. The WRF model solves the compressible non-hydrostatic Euler equations presented in flux form on a mass-based terrain-following vertical coordinate system. Predicted variables include the WV mixing ratio, vertical and horizontal wind components, the mixing ratios and number concentrations for several cloud microphysical species, and perturbations in potential temperature, surface pressure of dry air, and geopotential height. The reader is referred to *Skamarock et al.* [2005] for a detailed description of the WRF modeling system.

2.2. Data Assimilation System

[8] Ensemble data assimilation experiments were performed using the Data Assimilation Research Testbed (DART) [*Anderson et al.*, 2009] system developed at the National Center for Atmospheric Research. The ensemble adjustment Kalman filter algorithm [*Anderson*, 2001] used during this study processes observations serially and is mathematically equivalent to the ensemble square root filter developed by *Whitaker and Hamill* [2002]. Temporally and spatially varying covariance inflation values at each grid point are automatically computed during the assimilation step using the methodology described by *Anderson* [2007, 2009]. Sampling errors resulting from the rank-deficient ensemble size are reduced using vertical and horizontal covariance localization [*Mitchell et al.*, 2002; *Hamill et al.*, 2001; *Houtekamer et al.*, 2005] based on a compactly supported fifth-order correlation function [*Gaspari and Cohn*, 1999].

2.3. Satellite Brightness Temperature Forward Model Operator

[9] Simulated infrared brightness temperatures are computed using the Successive Order of Interaction (SOI) forward radiative transfer model [*Heidinger et al.*, 2006; *O'Dell et al.*, 2006]. The SOI model uses CompactOPTRAN code from the Community Radiative Transfer Model (CRTM) [*Han et al.*, 2006] to compute gas optical depths for each model layer. Absorption and scattering properties, such as the full scattering phase function, single scatter albedo, and extinction efficiency, for each frozen hydrometeor species (i.e., ice, snow, and graupel) are obtained from *Baum et al.* [2005], whereas a lookup table based on Lorenz-Mie calculations is used for the liquid species (i.e., cloud water and rainwater). Visible cloud optical depths are calculated for each microphysical species based on *Han et al.* [1995] and *Heymsfield et al.* [2003], and then converted into infrared

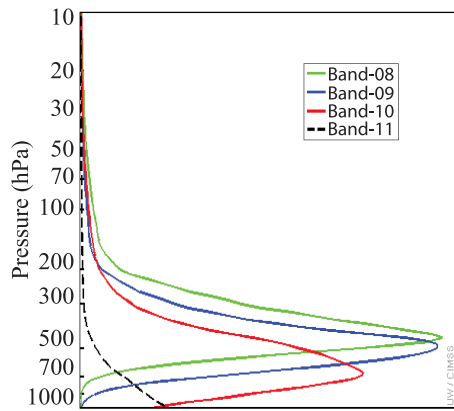


Figure 1. Clear-sky weighting function profiles for ABI bands 8–11 plotted for a midlatitude winter atmosphere at a satellite zenith angle of 40° . The weighting functions were calculated using simulated spectral response functions based on proposed ABI bandwidths.

cloud optical depths by scaling the visible optical depths by the ratio of the extinction efficiencies. The surface emissivity for each ABI infrared band is obtained from the *Seemann et al.* [2008] global emissivity database for land grid points; however, for water points, the CRTM Infrared Sea Surface Emissivity Model is used to compute the surface emissivity. WRF model data used by the SOI model to compute simulated brightness temperatures includes the WV mixing ratio, atmospheric temperature, surface skin temperature, 10-m wind speed, and the mixing ratios for each hydrometeor species predicted by the microphysics parameterization scheme. Previous studies have shown that the SOI model computes accurate infrared brightness temperatures for both clear and cloudy sky conditions [Otkin and Greenwald, 2008; Otkin et al., 2009].

[10] To assimilate satellite observations, Otkin [2010] wrote an interface between the SOI forward model and the DART system. Although the SOI model is very complex, it is still treated the same as any other observation operator in DART, which is an important benefit of using ensemble data assimilation systems to assimilate complex observations. At the end of each forecast cycle, output from the nearest model grid point to a given observation location is passed from each ensemble member to the forward model, which is then used to compute the simulated brightness temperatures for the entire ensemble. These values are subsequently returned to the main DART program used to assimilate all observations.

2.4. Simulated Observations

[11] Data from the high-resolution (6-km) “truth” simulation described in Section 3 was used to generate simulated observations for the ABI sensor and three conventional in situ observing systems, including radiosondes, the Aircraft Communications Addressing and Reporting System (ACARS), and the Automated Surface Observing System (ASOS). Simulated surface pressure, 2-m temperature and relative humidity, and 10-m wind speed and direction observations were computed for each ASOS station. Vertical profiles of temperature, relative humidity, and horizontal wind speed and direction were generated for mandatory and significant levels at each radiosonde location following standard

reporting conventions. Simulated ACARS wind and temperature observations were computed for the same flight level and location as the real pilot reports listed in the Meteorological Assimilation Data Ingest System files during the case study period.

[12] The SOI forward radiative transfer model was used to compute simulated infrared brightness temperatures for three ABI bands that are sensitive to the WV content in the upper troposphere (band 8; $6.19 \mu\text{m}$), middle troposphere (band 9; $6.95 \mu\text{m}$), and lower troposphere (band 10; $7.34 \mu\text{m}$). These bands are also sensitive to clouds if they are located near or above the peak in the weighting function profile for each band (refer to Figure 1). For comparison to prior work by Otkin [2010, 2012], simulated brightness temperatures were also computed for band 11 ($8.5 \mu\text{m}$), which is a standard window channel that is sensitive to cloud top properties when clouds are present or to the surface when the sky is clear. Figure 1 shows the theoretical weighting function profiles for each band under clear sky conditions for a midlatitude cool season atmosphere at a satellite zenith angle of 40° . A weighting function profile specifies the relative contribution from each atmospheric layer to the radiation emitted to space and thereby determines those regions of the atmosphere that are sensed from space at a given wavelength. The ABI observations were computed on the 6-km “truth” grid and were then averaged to 30 km resolution prior to assimilation. Averaged observations were only used if all of the grid points within each averaging area on the truth domain were either clear or cloudy, thus partly cloudy averaged observations were not assimilated during this study. A grid point was considered cloudy if the cloud optical thickness for any of the predicted microphysical species was greater than zero.

2.5. Measurement and Observation Errors

[13] Realistic measurement errors drawn from an uncorrelated and unbiased Gaussian error distribution with unit variance were added to each observation. Table 1 shows the maximum measurement errors allowed for each observation type. Measurement errors can be due to systematic biases resulting from limited sensor accuracy in some or all situations or they can be due to random errors in the observations. To account for other sources of uncertainty, such as numerical model bias and representativeness errors, the observation errors used during the assimilation step are typically much larger than the actual measurement errors, particularly for observations that are sensitive to the WV and cloud fields. For the conventional observations, the observation errors are similar to those used operationally at the National Center for Environmental Prediction (NCEP). The temperature and wind component errors for the ACARS observations were set to 1.8 K and 3.8 m s^{-1} . At the surface, errors for the ASOS observations were set to 1.5 hPa for the surface pressure, 2 K and 18% for the 2-m temperature and relative humidity, and 3.5 m s^{-1} for the 10-m zonal and meridional wind components. The radiosonde errors were a function of height and varied from 10 to 15% for relative humidity, 0.8 – 1.2 K for temperature, and 1.4 – 3.2 m s^{-1} for the zonal and meridional wind components. For the ABI brightness temperatures, the observation error was set to 2.5 K , 2.8 K , 3.5 K , and 5 K for bands 8, 9, 10, and 11, respectively, for both clear and cloudy observations. These

Table 1. Maximum Measurement Errors Used for Each Observation Type^a

Sensor	Observation Type	Maximum Measurement Error
ABI Radiosonde	Brightness Temperature	1 K
	Temperature	0.2 K
	Relative Humidity	2%
	Wind Speed	0.3 m s ⁻¹
	Wind Direction	0.15 degrees
ASOS	Temperature	0.8 K
	Dew Point Temperature (Td)	2.6 K for Td > 273 K; 4.4 K for Td < 273 K
	Wind Speed	1.0 m s ⁻¹ or 5% of the wind speed, whichever is greater
	Wind Direction	10 degrees for wind speeds <2.5 m s ⁻¹ ; 5 degrees for wind speeds >2.5 m s ⁻¹
	Surface Pressure	0.67 hPa
ACARS	Temperature	0.6–0.9 K
	Wind Speed	1.4–2.4 m s ⁻¹

^aThe errors were drawn from an uncorrelated and unbiased Gaussian error distribution with unit variance.

values were chosen after evaluating results from sensitivity tests in which the observation errors were systematically varied. The observation error used for the 8.5 μm brightness temperatures (band 11) is similar to that used by prior assimilation studies [e.g., *Seaman et al.*, 2010; *Otkin*, 2010, 2012]. Larger observation errors are necessary for bands with weighting functions peaking lower in the troposphere (refer to Figure 1) since their sensitivity to a greater depth of the atmosphere results in a greater range in brightness temperature values and thus potentially to larger representativeness errors.

3. Truth Simulation

[14] A truth simulation depicting the evolution of a strong midlatitude cyclone and associated areas of heavy precipitation across the central U.S. on 24 December 2009 was performed using the WRF model. Global 0.5° FNL (final) analyses from NCEP were used to initialize the simulation at 00 UTC on 23 December 2009 on a 1100 × 750 grid point domain covering the contiguous U.S. with 6-km horizontal grid spacing and 52 vertical levels (Figure 2). The vertical grid spacing in the model decreased from <100 m in the lowest km to ~700 m near the model top at 10 hPa. A larger horizontal domain was used for the truth simulation than for the assimilation experiments to reduce the impact of the lateral boundary conditions on the atmospheric state over the contiguous U.S. The WRF Single Moment 6-Class mixed-phase microphysics scheme [*Hong and Lim*, 2006], the Yonsei University planetary boundary layer scheme [*Hong et al.*, 2006], the Kain-Fritsch cumulus scheme [*Kain and Fritsch*, 1993; *Kain*, 2004], and the RRTMG longwave and shortwave radiation schemes [*Iacono et al.*, 2008] were used to parameterize sub-grid scale processes. Heat and moisture fluxes at the surface were computed using the Noah land surface model.

[15] The evolution of the height and wind fields in the lower and upper troposphere, along with the simulated PWAT and cloud top pressure, for a 12-h period during the truth simulation starting at 06 UTC on 24 Dec 2009 is shown in Figure 3. Simulated observations from the first six hours will be assimilated during the experiments presented in Section 4, whereas the last six hours will be used to assess the forecast impact of the observations. At 06 UTC, a deep upper level trough was located across the western U.S. (Figure 3a) with a seasonably strong jet streak (55 m s⁻¹)

extending from northern Mexico into the southern U.S. Widespread ascent ahead of the trough led to an extensive area of cloud cover across the central U.S. Strong southerly winds in the lower troposphere were rapidly transporting very moist air northward across the lower Mississippi River Valley with PWAT values >2 cm as far north as southern Wisconsin (Figure 3b). By 12 UTC, a strong shortwave disturbance was emerging from the base of the trough over Texas (Figure 3c), while extensive moisture continued to stream northward into the central U.S. (Figure 3d). During the ensuing six hours, the shortwave trough acquired a large negative tilt (Figure 3e), while an intense surface cyclone and a well-defined low-level circulation developed across the Southern Plains (Figure 3f). A sharp moisture gradient occurred to the south of the cyclone as a strong cold front and much drier air moved across eastern Texas and the northern Gulf of Mexico.

4. Assimilation Results

4.1. Initial Ensemble and Model Configuration

[16] The assimilation experiments presented later in this section start at 06 UTC on 24 December 2009. Initial conditions valid at this time were created for a 60-member WRF model ensemble by adding perturbed initial and lateral

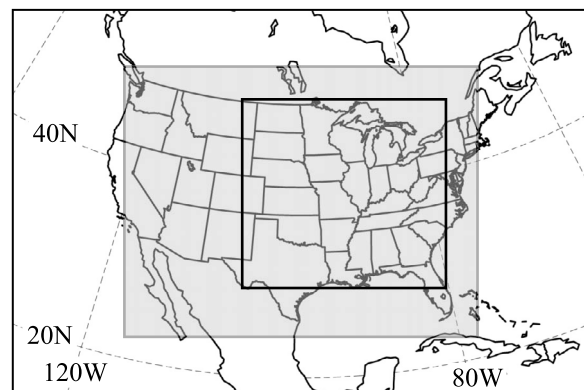


Figure 2. Geographical coverage of the 6-km truth domain. The shaded area corresponds to the domain used during the assimilation experiments. The inner black rectangle encloses the region used for the forecast verification in Section 5.

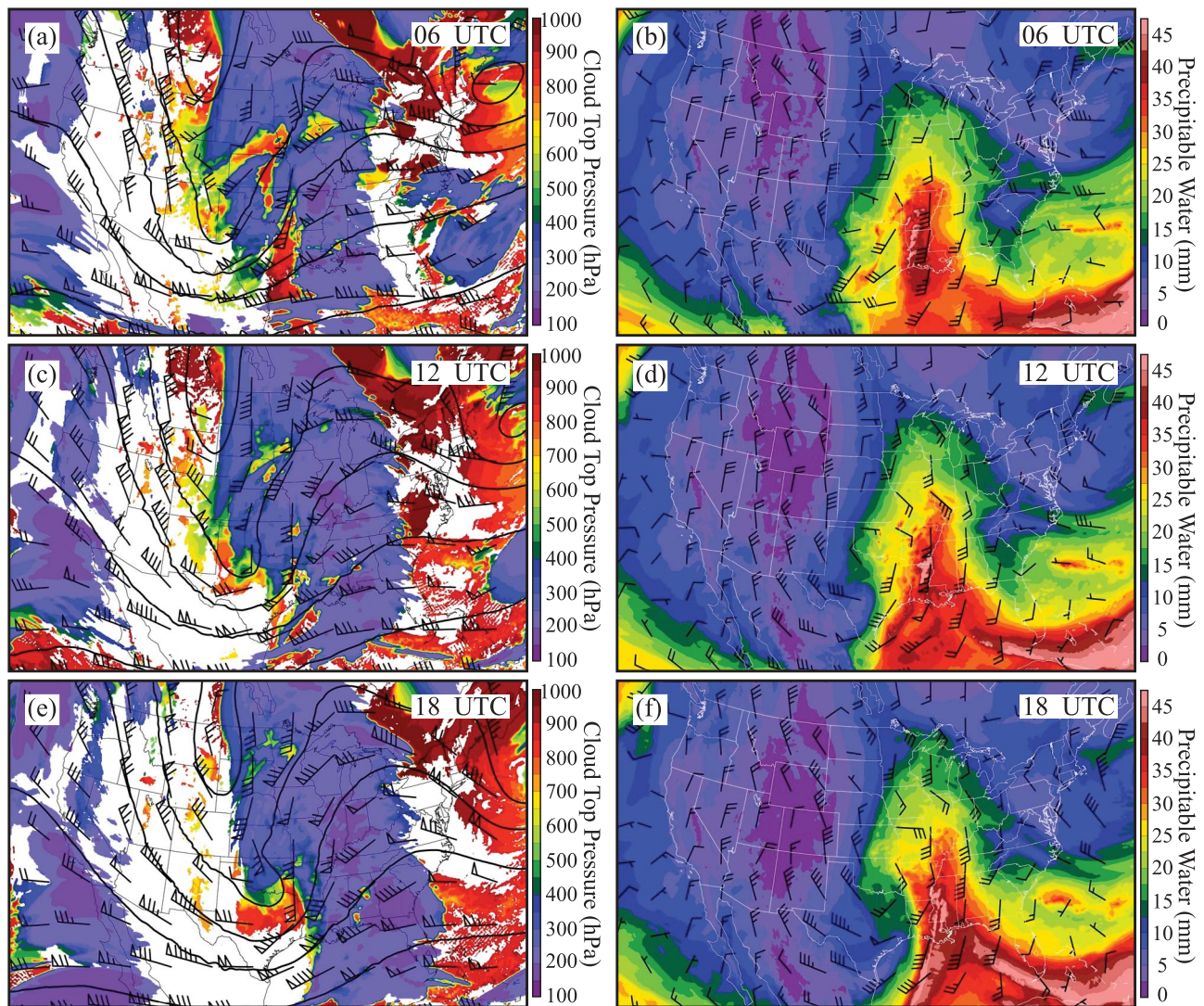


Figure 3. (a) Simulated cloud top pressure (hPa; color filled), 300 hPa geopotential height (m; contoured) and 300 hPa winds (m s^{-1}) valid at 06 UTC on 24 December 2009. Each wind barb equals 5 m s^{-1} . (b) Simulated total precipitable water (mm; color filled) and 700 hPa winds (m s^{-1}) valid at 06 UTC on 24 December 2009. Each wind barb equals 5 m s^{-1} . (c and d) Same as Figures 3a and 3b except for 12 UTC on 24 December 2009. (e and f) Same as Figures 3a and 3b except for 18 UTC on 24 December 2009.

boundary perturbations to 0.5°N analyses at 00 UTC on 23 Dec and then integrating the ensemble for 30 h to increase the ensemble spread. Covariance statistics provided by the WRF-Var data assimilation system were used to generate the ensemble perturbations similar to the approach described by *Torn et al.* [2006]. The assimilation experiments were performed on a 272×216 grid point domain with 15-km horizontal grid spacing and 37 vertical levels. The assimilation domain covered a subset of the geographic domain used during the truth simulation (refer to Figure 2). Sub-grid scale processes were parameterized using the same parameterization schemes as in the truth simulation.

[17] In the remainder of this section, results from five assimilation experiments that were designed to evaluate the impact of WV sensitive infrared brightness temperatures on the analysis and forecast accuracy will be compared to data from the truth simulation. Simulated conventional observations

were the only observations assimilated during the Control case, while both conventional observations and clear and cloudy-sky brightness temperatures were assimilated during the other cases. Observations from the ABI $6.19 \mu\text{m}$, $6.95 \mu\text{m}$, $7.34 \mu\text{m}$, and $8.5 \mu\text{m}$ spectral bands were assimilated separately during the Band-08, Band-09, Band-10, and Band-11 cases, respectively. Simulated radiosonde observations were assimilated at 12 UTC, whereas all other observations were assimilated every 30 min during a 6-h period from 06 UTC until 12 UTC on 24 Dec. The horizontal and vertical covariance localization radii were set to 600 km and 6 km, respectively, for the conventional observations. Sensitivity tests revealed that much smaller horizontal radii were necessary for the brightness temperature observations to account for their higher spatial resolution and the potential for larger uncertainties in the representativeness of small-scale cloud and WV features detected by infrared

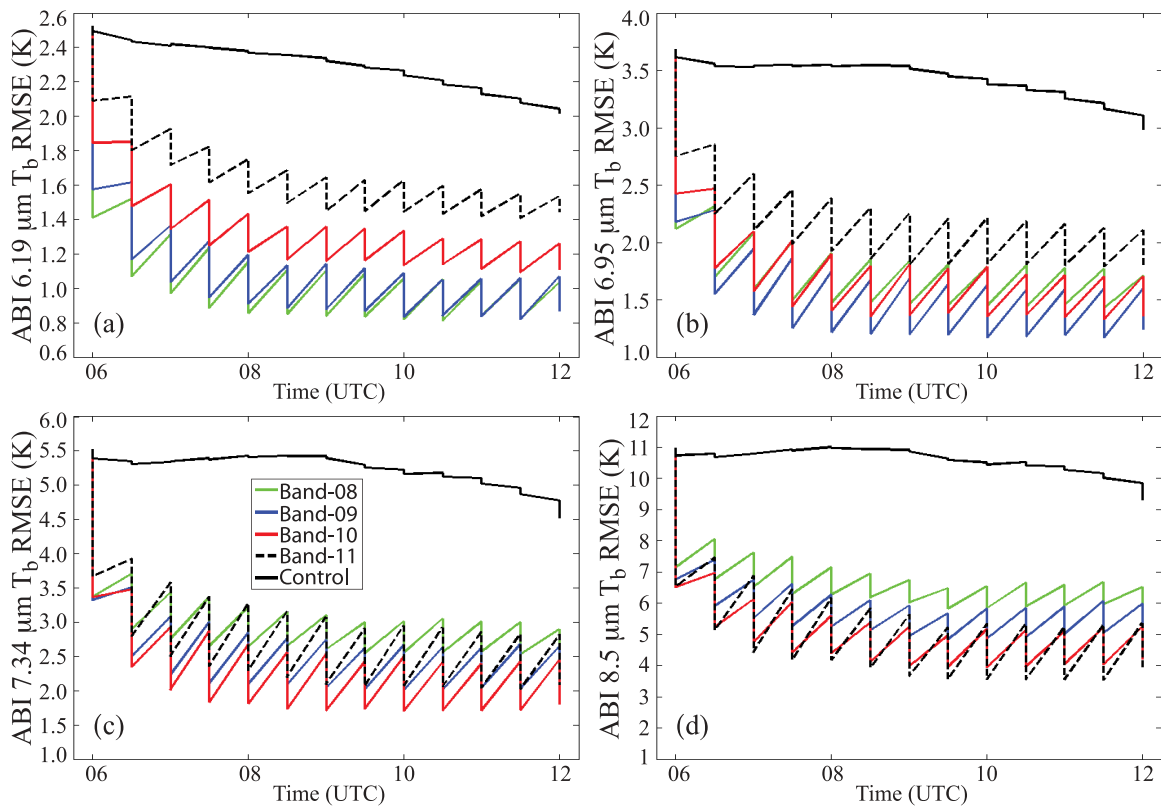


Figure 4. Time evolution of the ensemble mean forecast and analysis (sawtooth pattern) brightness temperature root mean square error (RMSE; K) from 06 UTC on 24 December to 12 UTC on 24 December for the ABI (a) 6.19 μm , (b) 6.95 μm , (c) 7.34 μm , and (d) 8.5 μm bands. Results are shown for the Band-08 (green), Band-09 (blue), Band-10 (red), Band-11 (dashed black) and Control (solid black) experiments.

sensors. The chosen radii are consistent with the results shown in *Otkin* [2012]. For these observations, the horizontal localization radius was set to 100 km for band 11 and to 200 km for bands 8, 9, and 10. Vertical covariance localization was not used for the brightness temperature observations since they are sensitive to broad layers of the atmosphere. The model state vector includes the surface pressure, WV mixing ratio, temperature, horizontal and vertical wind components, and the mixing ratios for cloud water, rainwater, pristine ice, snow, and graupel. Covariance inflation at each grid point was computed using the time and spatially varying inflation scheme developed by *Anderson et al.* [2009].

4.2. Time Series Error Analysis

[18] Figure 4 shows the temporal evolution of the prior and posterior root mean square errors (RMSE) for the ABI 6.19 μm , 6.95 μm , 7.34 μm , and 8.5 μm bands for each assimilation cycle during the 6-h assimilation period. Output from the truth simulation was averaged to 15-km resolution prior to computing the statistics in order to match the resolution of the assimilation grid. Although the magnitude of the error statistics will decrease for each case due to the removal of the local maxima and minima in the truth simulation, this is acceptable since it will lessen the impact of small-scale cloud and WV features in the truth simulation that are simply not reproducible on the coarser resolution assimilation grid. Overall, the RMSE was much lower

during the brightness temperature assimilation cases, with the smallest errors for a given band occurring when observations from that band were assimilated. Large error reductions occurred during the first several assimilation cycles with nearly constant errors after 09 UTC. The lower errors during the brightness temperature assimilation cases are partially due to a more accurate cloud top pressure analysis and a concomitant reduction in the negative bias that was present in the initial ensemble (not shown). Additional information about the moisture field contained in the Band-08, Band-09, and Band-10 observations; however, led to even lower errors for the WV sensitive bands (Figures 4a–4c) during those cases.

[19] To more closely examine the impact of the observations on the column-integrated cloud and moisture analyses, the evolution of the prior and posterior RMSE for the cloud water path (CWP) and PWAT fields is shown in Figure 5. Comparison of the brightness temperature assimilation cases shows that large improvements were made to the moisture and cloud analyses at each assimilation time regardless of which band was assimilated; however, the smallest errors tended to occur when Band-10 (7.34 μm) observations were assimilated. Given that the PWAT magnitude is closely related to the moisture content in the lower troposphere, it is not surprising that the RMSE decreases as the sensitivity of the WV bands moves from the upper troposphere (Band-08) to the lower troposphere (Band-10) simply because the lower-peaking channels will have a stronger influence where

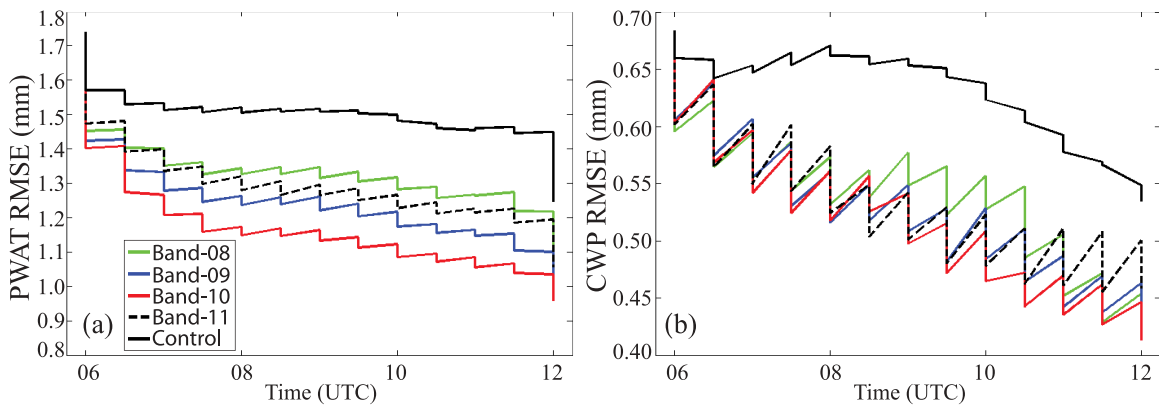


Figure 5. Time evolution of the ensemble mean forecast and analysis (sawtooth pattern) root mean square error (RMSE) from 06 UTC on 24 December to 12 UTC on 24 December for (a) precipitable water (PWAT; mm), and (b) cloud water path (CWP; mm). Results are shown for the Band-08 (green), Band-09 (blue), Band-10 (red), Band-11 (dashed black) and Control (solid black) experiments.

most of the WV is located. Even though Band-11 observations are not sensitive to moisture, their greater sensitivity to low-level clouds still led to lower PWAT errors due to the close relationship between clouds and moisture. The Band-08 errors are slightly larger than the Band-11 errors because they are not sensitive to clouds or WV in the lower troposphere, which makes it more difficult for them to have a larger impact on the integrated WV content. The especially large reduction in the PWAT RMSE at 12 UTC is due to the radiosonde humidity observations, which illustrates their important influence on the moisture analysis. All of the WV band experiments contained lower CWP errors (Figure 5b) than the Band-11 and Control cases, which is encouraging since this indicates that improvements made to the moisture field by these observations also contribute to a more accurate cloud analysis.

4.3. Regional Cloud and WV Analysis

[20] To further investigate the impact of the observations on the horizontal structure of the cloud and WV analyses, Figure 6 shows the CWP and PWAT differences for each assimilation case computed by subtracting the posterior ensemble mean from the truth simulation after the first assimilation cycle at 06 UTC. The CWP and PWAT differences for the prior ensemble mean used by all of the assimilation cases are also shown. Several large errors were present in the prior ensemble mean (Figures 6a and 6b), including large areas of excessive moisture surrounding eastern Kansas, along the Gulf Coast, and over parts of Georgia and South Carolina. Erroneously dry air was located over most of Texas with several smaller areas of drier air scattered across the domain. The cloud field associated with the developing cyclone over the central U.S. contained excessive cloud condensate along its northern periphery, especially over eastern Kansas, and insufficient CWP within the region of deeper moisture and convective activity over Arkansas. Assimilation of conventional observations during the Control case (Figures 6c and 6d) reduced the areal extent of the erroneously moist atmosphere surrounding eastern Kansas, but had minimal impact on the PWAT field elsewhere. Small improvements were also made to the CWP field, especially over eastern Kansas and the lower Ohio

River Valley. More substantial improvements were made to the cloud and WV analyses when the WV-sensitive brightness temperatures were assimilated (Figures 6e–6j). For instance, these observations were able to more efficiently reduce the cloud condensate errors in the northwestern third of the cloud shield over the central U.S., while simultaneously increasing the CWP magnitude within the convective band further to the southeast. Compared to the Control case, additional drying also occurred within the erroneously moist areas over eastern Kansas and along the Gulf Coast, while some moistening occurred within the drier air over Texas. Several small areas of slight degradation occurred in the PWAT field over southern Missouri and Arkansas where the observations exacerbated errors present in the prior ensemble analysis. When Band-11 observations were assimilated (Figures 6k and 6l), similar improvements were noted in the CWP and PWAT fields; however, the errors tended to be slightly larger than occurred during the WV assimilation cases.

[21] By the end of the assimilation period at 12 UTC (Figure 7), large PWAT errors, both negative and positive, remained across the southern half of the domain during the Control case (Figure 7a). Excessive cloud condensate also persisted across the northwestern half of the cloud shield from Oklahoma to southern Wisconsin, while a narrow band associated with a line of deep convection along the Mississippi River contained too little CWP (Figure 7b). Overall, these errors were much smaller when the WV sensitive observations were assimilated during the Band-08, Band-09, and Band-10 cases (Figures 7c–7h). Although the locations and spatial extent of the PWAT errors were very similar in the WV cases, their magnitude generally decreased from the Band-08 to Band-10 cases, which is consistent with the time series results in Figure 5. Over the southeastern U.S., this tendency was beneficial for most areas, but did lead to the removal of too much PWAT over western Georgia during the Band-10 case due to excessive drying in the lower troposphere. The WV-sensitive brightness temperatures were also able to effectively remove most of the dry bias across Texas. Inspection of the Band-11 results (Figures 7i and 7j) shows that the final PWAT and CWP analyses were generally better than the Control case,

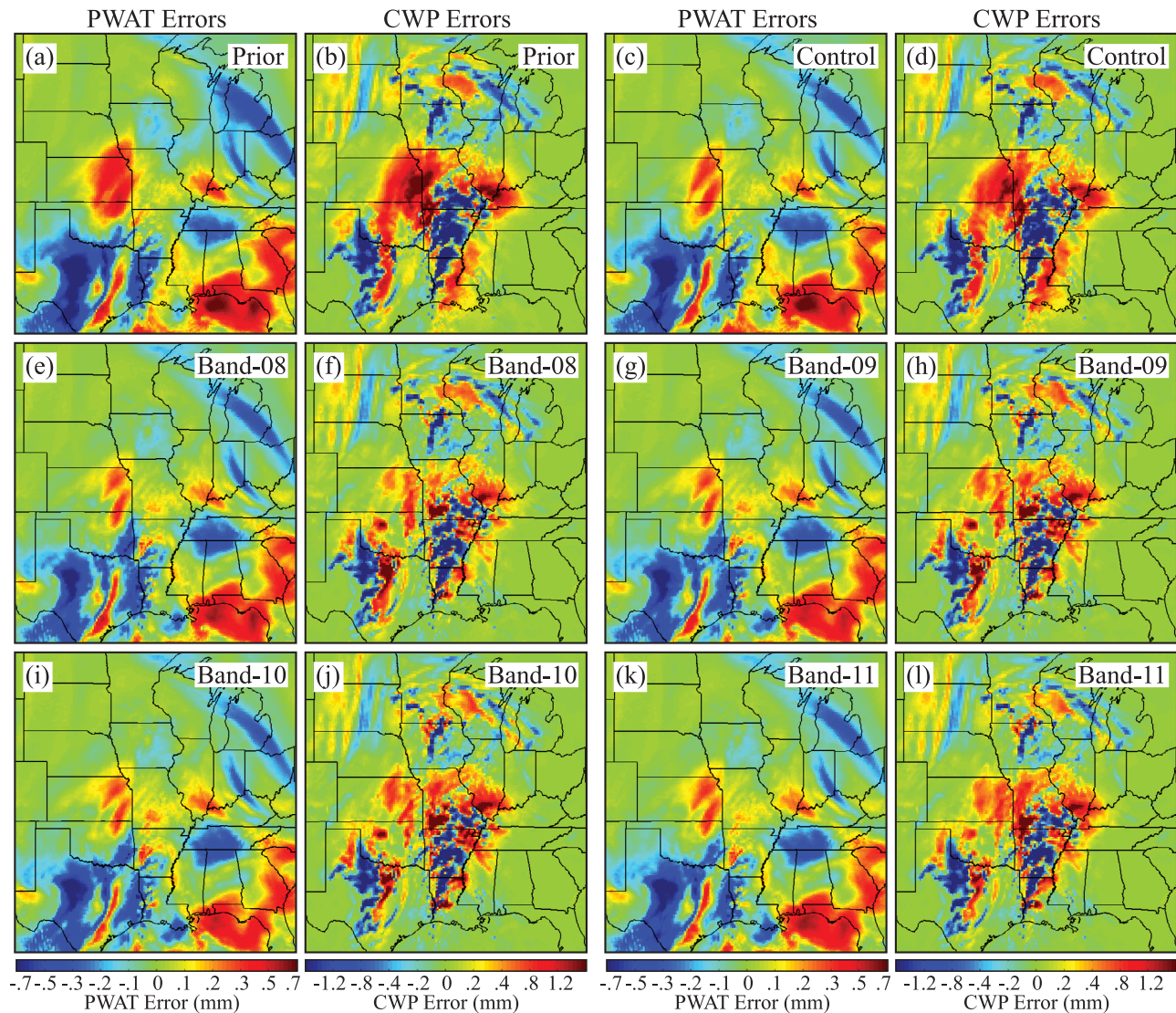


Figure 6. (a) Precipitable water (mm) and (b) cloud water path (mm; sum of cloud water, rainwater, pristine ice, snow, and graupel) analysis errors computed by subtracting the prior ensemble mean analysis from the truth simulation at 06 UTC on 24 December 2009. (c and d) Same as Figures 6a and 6b except for the Control case posterior ensemble mean analysis. (e and f) Same as Figures 6c and 6d except for the Band-08 case. (g and h) Same as Figures 6a and 6b except for the Band-09 case. (i and j) Same as Figures 6c and 6d except for the Band-10 case. (k and l) Same as Figures 6c and 6d except for the Band-11 case.

but not as accurate as the WV band assimilation cases. This behavior again indicates that WV sensitive infrared brightness temperatures are able to positively impact the cloud field as much as $8.5 \mu\text{m}$ observations, yet also provide much more information about the moisture distribution.

4.4. Final Analysis Accuracy

[22] The accuracy of the final analysis obtained after 6 h of assimilation is assessed in this section. Figure 8 shows vertical profiles of RMSE for relative humidity, total cloud hydrometeor mixing ratio (QALL; sum of the cloud water, rainwater, pristine ice, snow, and graupel mixing ratios), temperature, and vector wind speed. The statistics were computed for each case using data from the posterior ensemble mean at 12 UTC on 24 Dec, excluding the outermost 25 grid

points of the assimilation domain. Compared to the Control case, the relative humidity, QALL, and vector wind analyses were all greatly improved during the brightness temperature assimilation cases. With the exception of the upper troposphere, the temperature analysis was also more accurate during these cases. The relatively weak sensitivity of the infrared observations in the upper troposphere (as inferred from the weighting function profiles in Figure 1) likely contributed to the presence of less accurate temperature analyses, particularly for infrared bands peaking lower in the troposphere, such as Band-10 and Band-11. Overall, the analyses for the WV band assimilation cases were better than those for the Band-11 case, particularly in the middle and upper troposphere. Comparison of the WV band results shows that the temperature and vector

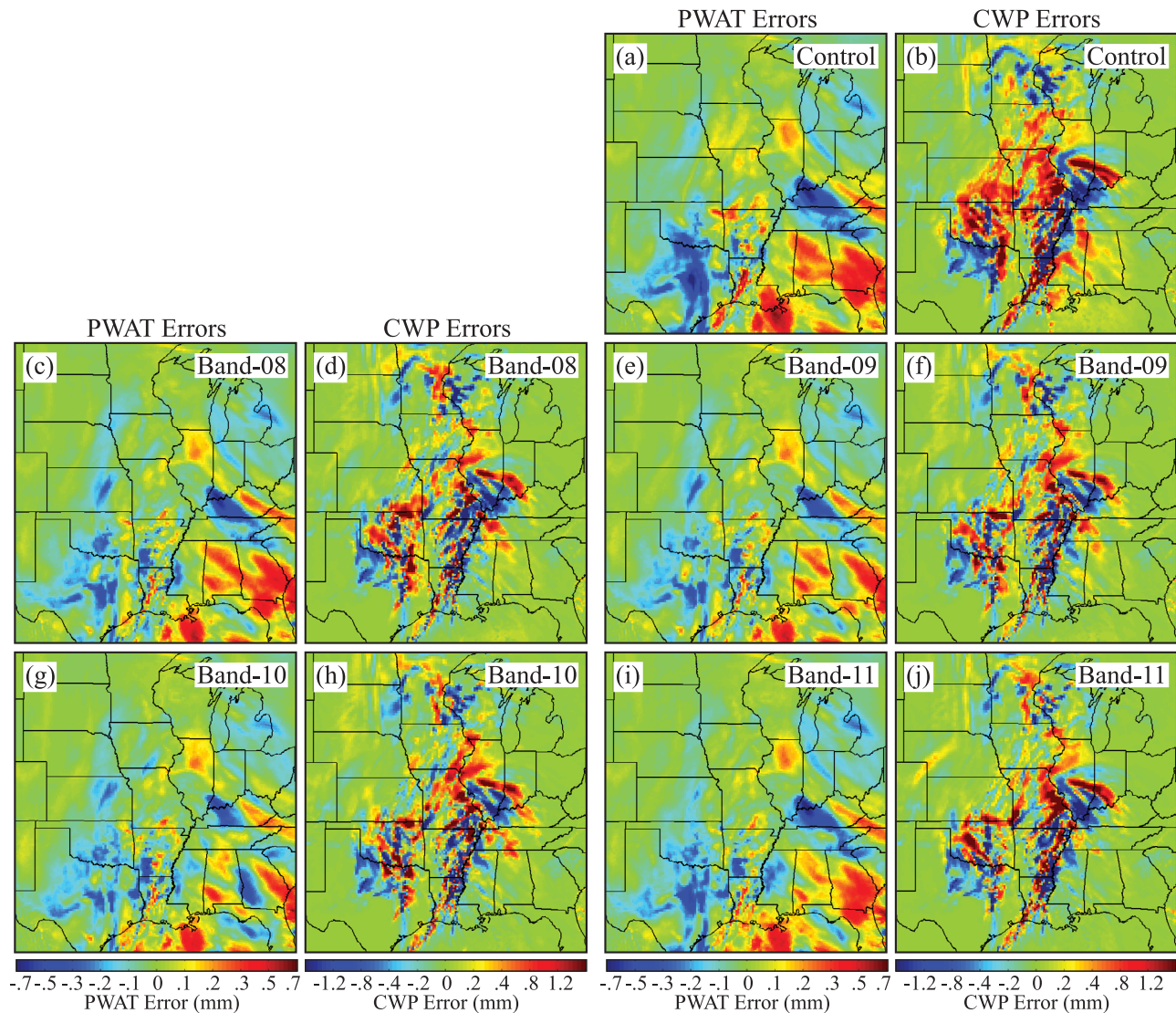


Figure 7. (a) Precipitable water (mm) and (b) cloud water path (mm; sum of cloud water, rainwater, pristine ice, snow, and graupel) errors for the Control case computed by subtracting the posterior ensemble mean analysis from the truth simulation at 12 UTC on 24 December 2009. (c and d) Same as Figures 7a and 7b except for the Band-08 case. (e and f) Same as Figures 7a and 7b except for the Band-09 case. (g and h) Same as Figures 7a and 7b except for the Band-10 case. (i and j) Same as Figures 7a and 7b except for the Band-11 case.

wind analyses were most improved when Band-08 observations were assimilated; however, the errors were smaller for the cloud and moisture fields during the Band-09 and Band-10 cases. Aside from the QALL analysis, the improvements during the Band-08 case were especially large above 400 hPa, most likely due to the greater sensitivity of these observations to WV in the upper troposphere.

[23] In summary, the results from Section 4 indicate that the $6.95 \mu\text{m}$ (Band-09) and $7.34 \mu\text{m}$ (Band-10) WV sensitive brightness temperature observations had the largest positive impact on the moisture and cloud fields, while the thermodynamic fields were most accurate when the $6.19 \mu\text{m}$ (Band-08) brightness temperatures were assimilated. All of the WV band cases were generally more accurate than the $8.5 \mu\text{m}$ (Band-11) results and were much more accurate than

when only conventional observations were assimilated during the Control case.

5. Forecast Impact

5.1. Mean Error Profiles

[24] To assess the impact of the observations on the short-range model forecast skill during this high-impact weather event, 6-h ensemble forecasts were performed for each case using the final ensemble analyses from 12 UTC on 24 Dec. Figure 9 shows vertical profiles of RMSE for temperature, relative humidity, and vector wind speed for the 1, 3, and 6-h forecast times. Data from the ensemble mean for the sub-domain shown in Figure 2 were used to compute the statistics. A smaller area was used to evaluate the forecast accuracy to limit the impact of the lateral boundary conditions on

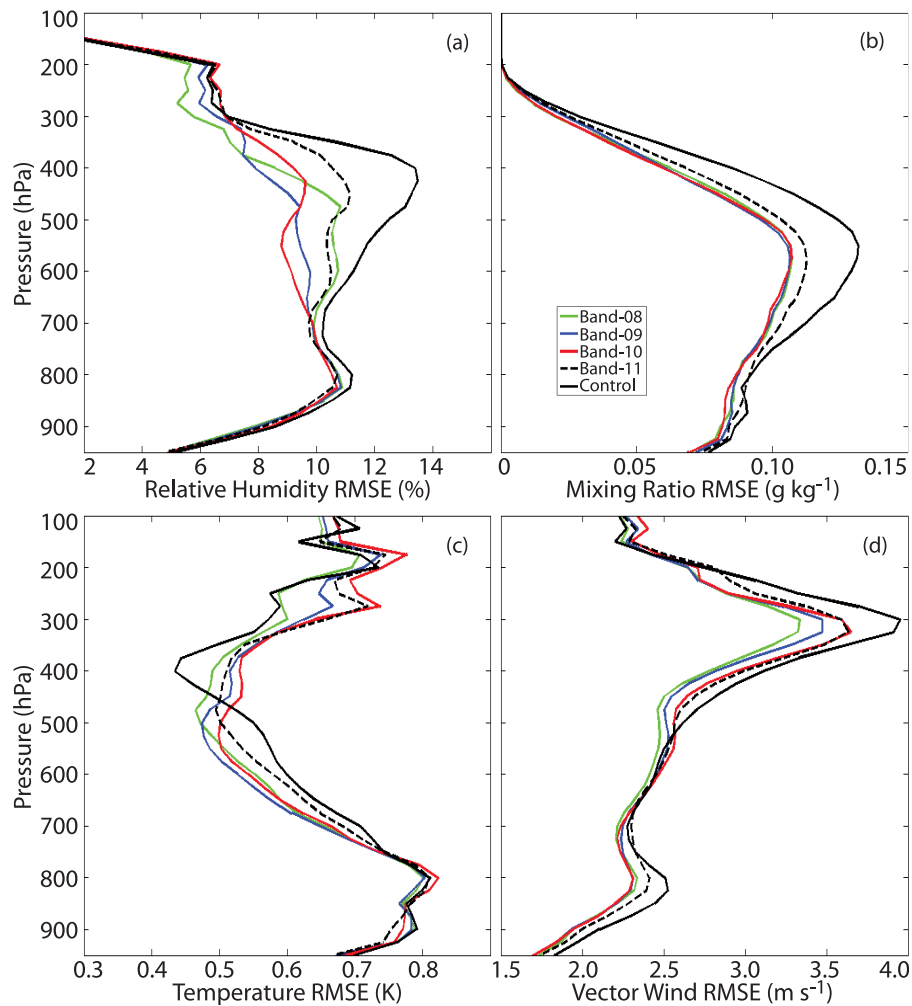


Figure 8. Vertical profiles of root mean square error for (a) relative humidity (%), (b) total cloud hydrometeor mixing ratio (g kg^{-1} ; sum of cloud water, rainwater, cloud ice, snow, and graupel), (c) temperature (K), and (d) vector wind speed (m s^{-1}). The profiles were computed using data from the posterior ensemble mean at 1200 UTC on 24 January 2009. Results are shown for the Band-08 (green), Band-09 (blue), Band-10 (red), Band-11 (dashed black) and Control (solid black) experiments.

the forecast statistics. Overall, improvements made to the moisture and thermodynamic analyses during the brightness temperature assimilation cases persisted during the forecast period. For the WV band cases, the most accurate analyses in the upper troposphere occurred during the Band-08 case; however, the errors were smaller in the lower troposphere during the Band-09 and Band-10 cases, which is consistent with the analysis results shown in Figure 8. Errors during the WV band forecasts were generally less than those during the Band-11 and Control cases, especially for the temperature and relative humidity fields. Since the error spread between the WV band and Control cases tended to increase with time, this indicates that the error growth was better constrained when WV-sensitive infrared brightness temperatures were assimilated.

[25] Vertical profiles showing the reduction in the moisture flux convergence (MFC) RMSE for each brightness temperature assimilation case relative to the Control case are displayed in Figure 10 for the beginning, middle, and end of the forecast period. Improved MFC forecasts require a more accurate depiction of the moisture and wind fields and are

necessary to better predict the location and intensity of surface precipitation. The MFC RMSE was much lower during the brightness temperature assimilation cases at all levels and for all forecast times, with error reductions $>10\%$ common throughout the depth of the troposphere. Although large improvements occurred during the Band-11 case, the errors were even lower during the WV band forecasts, which is consistent with the more accurate moisture and wind forecasts during these cases. Comparison of the WV band results shows that the MFC errors were typically lowest for the Band-09 and Band-10 cases. Their superior performance compared to the Band-08 case indicates that the larger improvements in the relative humidity field during these cases were more important for the MFC forecast than the more accurate vector wind forecast was during the Band-08 case.

5.2. Accumulated Precipitation Forecasts

[26] The 6-h accumulated precipitation from 12 UTC until 18 UTC on 24 Dec is shown in Figure 11 for the truth

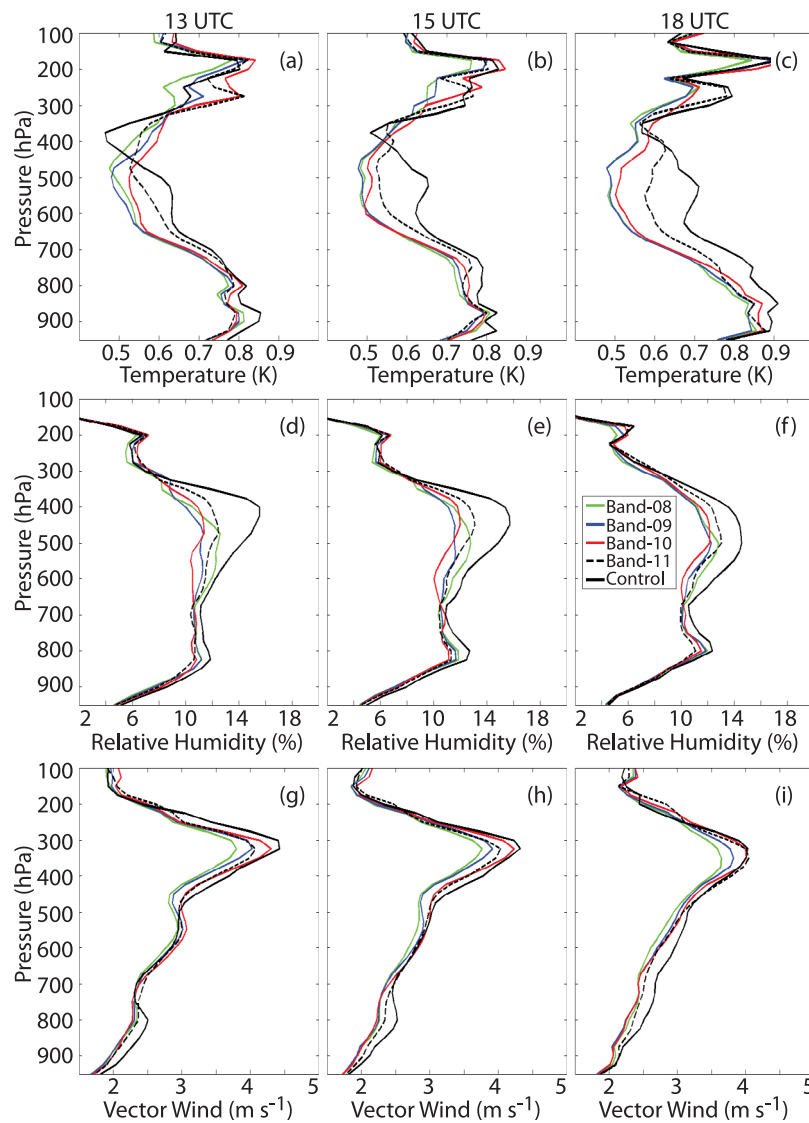


Figure 9. Temperature forecast root mean square error (K) profiles valid at (a) 13 UTC, (b) 15 UTC, and (c) 18 UTC on 24 December 2009. (d, e, and f) Same as Figures 9a, 9b, and 9c except for relative humidity (%). (g, h, and i) Same as Figures 9a, 9b, and 9c except for vector wind (m s^{-1}). Statistics were computed using data from the ensemble mean. Results are shown for the Band-08 (green), Band-09 (blue), Band-10 (red), Band-11 (dashed black) and Control (solid black) experiments.

simulation and for each assimilation case. Two areas of heavier precipitation were present in the truth simulation (Figure 11a), including a narrow band of snow extending from north central Texas to eastern Iowa, and an elongated area of very heavy rainfall associated with deep convection along the Mississippi River. The combination of very heavy snowfall and strong winds across north central Texas and Oklahoma lead to the development of extremely dangerous blizzard conditions that severely impacted holiday travel across the region. During the Control case (Figure 11b), the magnitude and spatial extent of the heavy rainfall area was generally well predicted; however, the precipitation forecast was too low across the heavy snowfall area and too high further to the north over northeastern Kansas and Iowa. The

precipitation forecasts across the heavy snowfall area were much better during the WV band cases (Figures 11c–11e). Similar improvements occurred during the Band-11 case (Figure 11f), though the heaviest snowfall area was shifted too far to the north. Much less snowfall occurred over northern Missouri and Iowa during the brightness temperature assimilation cases, which improved forecasts of the aerial coverage of the heaviest snowfall band, but led to maximum precipitation amounts that were slightly less than observed. Close inspection of the heavy rainfall area along the Mississippi River shows that some improvements also occurred across this region during the WV band cases. For instance, the rainfall band was narrower across northeastern Arkansas, yet the heaviest precipitation area to the south was

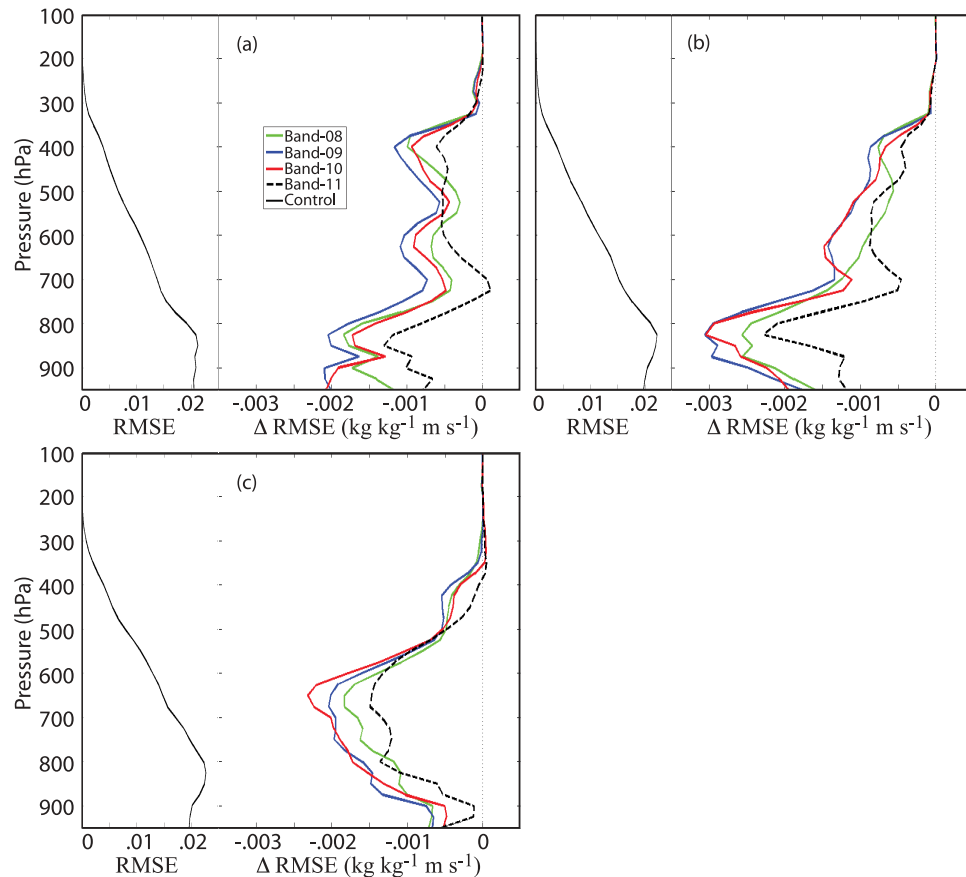


Figure 10. (a) Vertical profiles of moisture flux vector root mean square error reduction ($\text{kg kg}^{-1} \text{m s}^{-1}$) computed by subtracting the error profile for a given case from the Control case profile shown on the left side of the panel. The profiles were computed using data from the 0-h ensemble mean analysis valid at 1200 UTC 24 December 2011 in the forecast verification region shown in Figure 2. (b) Same as Figure 10a except valid at 1500 UTC 24 December. (c) Same as Figure 10a except valid at 1800 UTC 24 December. Results are shown for the Band-08 (green), Band-09 (blue), Band-10 (red), and Band-11 (dashed black) experiments.

wider than occurred during the Control case, both of which more closely resembled the truth simulation.

[27] To provide a quantitative measure of the precipitation forecast skill for each case, equitable threat scores [*Gandin and Murphy, 1992*] are shown for multiple precipitation thresholds in Table 2. As expected, the forecast skill was consistently higher for all precipitation thresholds during the WV band cases. For the lowest thresholds, the highest skill occurred during the Band-08 case; however, for heavier precipitation amounts, the skill was higher during the Band-09 and Band-10 cases. The reversal in skill scores between lower and higher precipitation thresholds during the WV band cases may be indicative of the relative influence of the moisture and thermodynamic fields during precipitation generation processes. For instance, the more accurate moisture and MFC forecasts during the Band-09 and Band-10 cases likely improved the forecast skill for heavier precipitation thresholds more than the Band-08 case by modifying the amount of moisture available for cloud and precipitation development in the lower and middle troposphere. More accurate temperature and wind forecasts during the Band-08 case, however, may have exerted a stronger influence on the lighter precipitation amounts by improving the spatial

coverage of the entire precipitation field due to a more accurate depiction of the large-scale forcing mechanisms.

6. Conclusions and Discussion

[28] In this study, results from a regional-scale OSSE were used to examine how infrared brightness temperatures that are sensitive to atmospheric WV and clouds impact the analysis and forecast accuracy during a high impact weather event. The OSSE case study tracked the evolution of a strong midlatitude cyclone and associated areas of heavy precipitation that developed across the central U.S. during 24 Dec 2009. A high-resolution “truth” simulation containing realistic cloud, moisture, and thermodynamic features was performed using the WRF model. Data from this simulation was used to generate synthetic ABI brightness temperatures for three bands that are sensitive to the WV content in the upper troposphere (band 8; $6.19 \mu\text{m}$), middle troposphere (band 9; $6.95 \mu\text{m}$), and lower troposphere (band 10; $7.34 \mu\text{m}$), and for one band that is sensitive to cloud top properties when clouds are present or to the surface when clouds are absent (band 11; $8.5 \mu\text{m}$). Each WV band is also sensitive to the cloud field if the top of a cloud is located

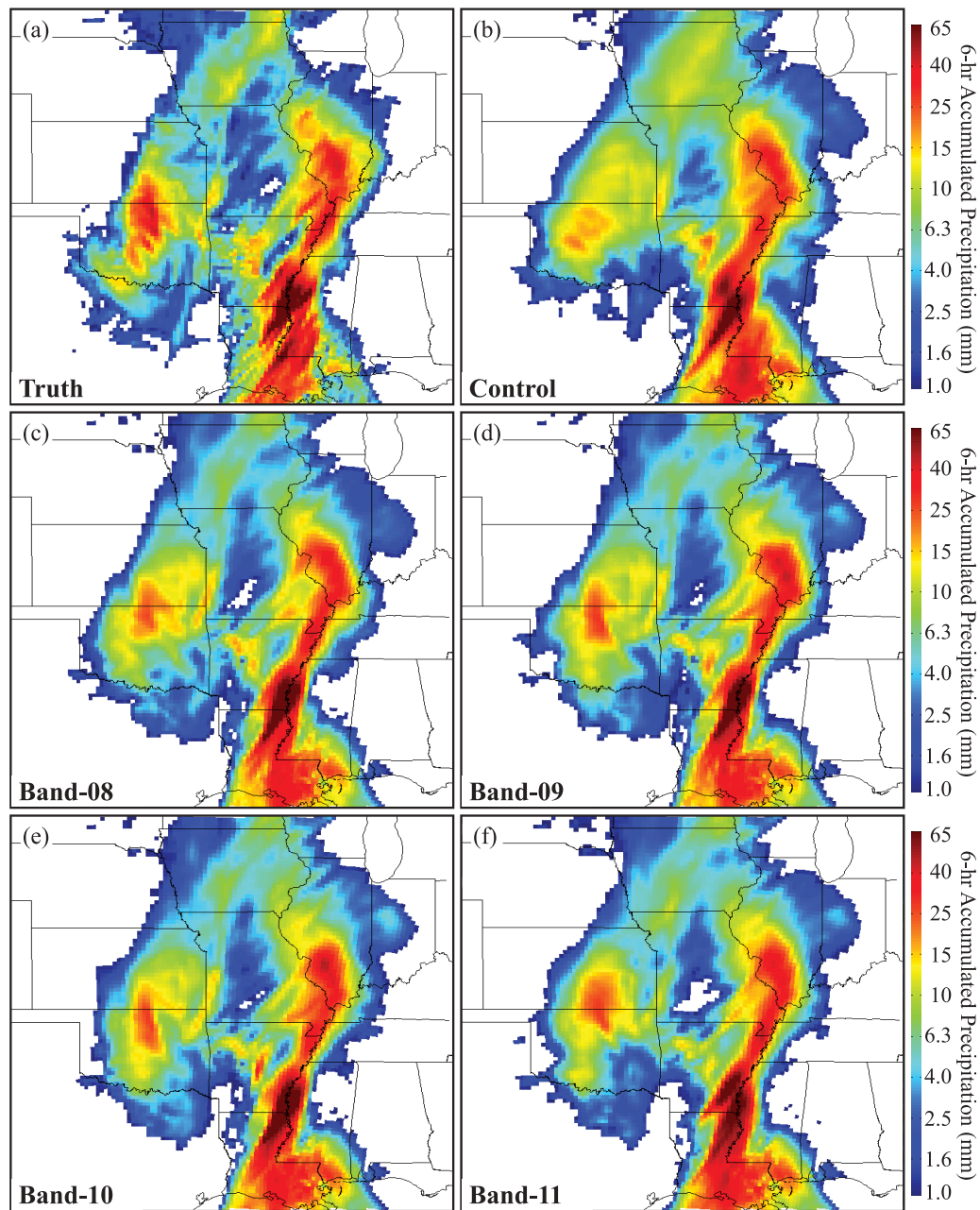


Figure 11. Accumulated precipitation (mm) from 12 UTC on 24 December to 18 UTC on 24 December for the (a) truth simulation, and for ensemble mean forecasts from the (b) Control, (c) Band-08, (d) Band-09, (e) Band-10, and (f) Band-11 experiments.

near or above the peak in the weighting function profile for a given band. Synthetic radiosonde, surface, and aircraft observations were also generated. Realistic errors based on a given sensor's accuracy specifications were added to each observation. Five assimilation experiments were performed using the EnKF algorithm in the DART assimilation system. Conventional observations were assimilated during the Control case, whereas both conventional and clear and cloudy-sky brightness temperatures were assimilated during the Band-08, Band-09, Band-10, and Band-11 cases. Observations were assimilated every 30 min during a 6-h period, with 6-h ensemble forecasts performed using the final ensemble analyses at the end of the assimilation period.

[29] Overall, the results showed that the analysis and forecast accuracy was greatly improved when infrared brightness temperatures were assimilated simultaneously with conventional observations. Comparison of the brightness temperature assimilation cases showed that large improvements were made to the WV analysis regardless of which band was assimilated; however, the smallest errors typically occurred during the Band-09 ($6.95 \mu\text{m}$) and Band-10 ($7.34 \mu\text{m}$) cases because of their greater sensitivity to moisture in the lower troposphere. Large WV errors present in the initial ensemble across the southern half of the domain were more effectively removed when WV-sensitive brightness temperatures were assimilated. Vertical error profiles at

Table 2. Equitable Threat Scores for 6-h Accumulated Precipitation (mm) Ending at 18 UTC on 24 December 2009^a

Experiment	6-h Accumulated Precipitation Thresholds (mm)				
	>0.25	>2.54	>6.35	>12.7	>25.4
Total Events	10,749	5,946	3,152	1,599	580
Control	0.724	0.663	0.573	0.558	0.387
Band-08	0.758	0.702	0.604	0.575	0.439
Band-09	0.756	0.679	0.601	0.595	0.450
Band-10	0.739	0.667	0.609	0.599	0.429
Band-11	0.742	0.671	0.608	0.552	0.434

^aScores are shown for precipitation thresholds >0.25 mm, >2.54 mm, >6.35 mm, >12.7 mm, and >25.4 mm. Bold entries indicate which experiment had the highest forecast skill for each precipitation threshold.

the end of the assimilation period showed that the final temperature and vector wind analyses were most accurate during the Band-08 (6.19 μm) case; however, the cloud analysis was most improved during the Band-09 and Band-10 cases. The analyses for the Band-11 (8.5 μm) case were more accurate than the Control case, but were not as good as the WV band results. These results indicate that compared to the 8.5 μm brightness temperatures, the enhanced ability of the WV-sensitive brightness temperatures to improve not only the cloud field, but also the moisture, wind, and temperature fields, increases their utility within a data assimilation system.

[30] Inspection of the subsequent short-range ensemble forecasts showed that the improved moisture and thermodynamic analyses at the end of the WV band assimilation cases persisted during the forecast period. Although the most accurate forecasts in the upper troposphere occurred during the Band-08 case, assimilation of Band-09 and Band-10 observations lead to better forecasts in the lower troposphere. Because the wind and moisture forecasts were more accurate during the WV band cases, better MFC forecasts also occurred, with error reductions >10% over much of the troposphere. The MFC errors were smallest during the Band-09 and Band-10 cases, which indicates that the larger improvements in the relative humidity forecasts during these cases had a greater impact on the MFC forecast than the more accurate wind forecast did during the Band-08 case. The more accurate forecasts of the moisture and thermodynamic fields controlling the cloud evolution lead to consistently higher equitable threat scores for all precipitation thresholds during the WV band cases. The Band-08 case had the highest skill scores for the lower thresholds; however, for higher precipitation amounts, the forecast skill was better during the Band-09 and Band-10 cases.

[31] Overall, the results showed that the assimilation of WV-sensitive infrared brightness temperatures had a large positive impact on both the analysis and forecast accuracy during this high-impact weather event. Since the OSSE framework adopted during this study provides a controlled environment with an absolute measure of the true state of the atmosphere (i.e., the truth simulation), it aids and simplifies the investigation of the observation impact, but it does not fully represent an operational environment. For instance, only a small subset of the observation types routinely assimilated at operational forecast centers were employed during this study and no attempt was made to assimilate observations from microwave sounders or hyperspectral infrared sensors

onboard polar-orbiting satellites. Although observations from these sensors have been shown to exert a positive impact on global numerical weather prediction, their utility within regional- and local-scale assimilation systems may decrease due to their much lower temporal sampling frequency. The value of geostationary sensors will increase for models with higher spatial resolution and more frequent assimilation cycles that better utilize their information content. Another important difference between this OSSE study and an operational environment is the treatment of surface emissivity over land, which can introduce significant errors for channels that are sensitive to the lower troposphere. This complication was avoided by using the same surface emissivity data set to generate the simulated ABI observations as was used during the assimilation experiments. Since errors in the specification of surface emissivity are most important for clear sky radiance assimilation, their negative impact would have been smaller during this study even if real observations had been assimilated simply because a majority of the infrared observations were cloudy and thus not sensitive to the surface characteristics. Last, it may also be necessary to account for observation bias, spatial error correlations between neighboring observations, and spectral correlations between channels with overlapping weighting function profiles when assimilating real satellite observations.

[32] Additional studies assimilating real infrared observations from the GOES imager and sounder are necessary to further enhance the utility of these important data sets for cloud and precipitation forecasting during high impact weather events. Attention should also be directed toward improving how observation errors are specified for clear and cloudy sky infrared observations. Prior work by *Otkin* [2012] indicated that the optimal error values for clear and cloudy observations may differ because of differences in their spatial variability and uncertainty in the underlying atmospheric fields. Similar results have also been found for cloudy sky microwave radiances [*Bormann et al.*, 2011; *Geer and Bauer*, 2011]. Last, given that infrared observations are most sensitive to the cloud top properties, whereas radar reflectivity and radial velocity observations are most sensitive to the internal cloud structure, a study is currently underway to explore the synergistic nature of these observations within an ensemble data assimilation system.

[33] **Acknowledgments.** This work was funded by the National Oceanic and Atmospheric Administration under grant NA10NES4400013. The assimilation experiments were performed using the NESDIS 'S4' supercomputer located at the University of Wisconsin-Madison and the 'ranger' supercomputer located at the Texas Advanced Computing Center. Ranger is part of the Extreme Science and Engineering Discovery Environment (XSEDE) network that is supported by the National Science Foundation under grant OCI-1053575. Comments from three anonymous reviewers improved the manuscript.

References

- Anderson, J. L. (2001), An ensemble adjustment Kalman filter for data assimilation, *Mon. Weather Rev.*, *129*, 2884–2903, doi:10.1175/1520-0493(2001)129<2884:AEAKFF>2.0.CO;2.
- Anderson, J. L. (2007), An adaptive covariance inflation error correction algorithm for ensemble filters, *Tellus, Ser. A*, *59*, 210–224.
- Anderson, J. L. (2009), Spatially and temporally varying adaptive covariance inflation for ensemble filters, *Tellus, Ser. A*, *61*, 72–83.
- Anderson, J., T. Hoar, K. Raeder, H. Liu, N. Collins, R. Torn, and A. Avellano (2009), The Data Assimilation Research Testbed: A community facility, *Bull. Am. Meteorol. Soc.*, *90*, 1283–1296, doi:10.1175/2009BAMS2618.1.

- Andersson, E., E. Holm, P. Bauer, A. Beljaars, G. A. Kelly, A. P. McNally, A. J. Simmons, J.-N. Thepaut, and A. M. Tompkins (2007), Analysis and forecast impact of the main humidity observing systems, *Q. J. R. Meteorol. Soc.*, *133*, 1473–1485.
- Baum, B. A., P. Yang, A. J. Heymsfield, S. Platnick, M. D. King, Y.-X. Hu, and S. T. Bedka (2005), Bulk scattering properties for the remote sensing of ice clouds. Part II: Narrowband models, *J. Appl. Meteorol.*, *44*, 1896–1911, doi:10.1175/JAM2309.1.
- Bormann, N., A. J. Geer, and P. Bauer (2011), Estimates of observation-error characteristics in clear and cloudy regions for microwave imager radiances from numerical weather prediction, *Q. J. R. Meteorol. Soc.*, *137*, 2014–2023, doi:10.1002/qj.833.
- Carlson, T. N., S. G. Benjamin, G. S. Forbes, and Y. F. Li (1983), Elevated mixed layers in the regional severe storm environment—Conceptual model and case studies, *Mon. Weather Rev.*, *111*, 1453–1474, doi:10.1175/1520-0493(1983)111<1453:EMLITR>2.0.CO;2.
- Donner, L. J. (1988), An initialization for cumulus convection in numerical weather prediction, *Mon. Weather Rev.*, *116*, 377–385, doi:10.1175/1520-0493(1988)116<0377:AIFCCI>2.0.CO;2.
- Evensen, G. (1994), Sequential data assimilation with a nonlinear quasi-geostrophic model using Monte Carlo methods to forecast error statistics, *J. Geophys. Res.*, *99*(C5), 10,143–10,162, doi:10.1029/94JC00572.
- Fabry, F., and J. Sun (2010), For how long should what data be assimilated for the mesoscale forecasting of convection and why? Part I: On the propagation of initial condition errors and their implications for data assimilation, *Mon. Weather Rev.*, *138*, 242–255.
- Gandin, L. S., and A. H. Murphy (1992), Equitable skill scores for categorical forecasts, *Mon. Weather Rev.*, *120*, 361–370, doi:10.1175/1520-0493(1992)120<0361:ESSFCF>2.0.CO;2.
- Gaspari, G., and S. E. Cohn (1999), Construction of correlation functions in two and three dimensions, *Q. J. R. Meteorol. Soc.*, *125*, 723–757, doi:10.1002/qj.4971255417.
- Geer, A. J., and P. Bauer (2011), Observation errors in all-sky data assimilation, *Q. J. R. Meteorol. Soc.*, *137*, 2024–2037, doi:10.1002/qj.830.
- Hamill, T. M., J. S. Whitaker, and C. Snyder (2001), Distance-dependent filtering of background error covariance estimates in an ensemble Kalman filter, *Mon. Weather Rev.*, *129*, 2776–2790, doi:10.1175/1520-0493(2001)129<2776:DDFOBE>2.0.CO;2.
- Han, Q., W. Rossow, R. Welch, A. White, and J. Chou (1995), Validation of satellite retrievals of cloud microphysics and liquid water path using observations from FIRE, *J. Atmos. Sci.*, *52*, 4183–4195, doi:10.1175/1520-0469(1995)052<4183:VOSROC>2.0.CO;2.
- Han, Y., P. van Delst, Q. Liu, F. Weng, B. Yan, R. Treadon, and J. Derber (2006), Community Radiative Transfer Model (CRTM): Version 1, *NOAA Tech. Rep. NESDIS 122*, 122 pp., NOAA, Washington, D. C.
- Heidinger, A. K., C. O'Dell, R. Bennartz, and T. Greenwald (2006), The successive-order-of-interaction radiative transfer model. Part I: Model development, *J. Appl. Meteorol. Climatol.*, *45*, 1388–1402, doi:10.1175/JAM2387.1.
- Heymsfield, A. J., S. Matrosov, and B. Baum (2003), Ice water path—optical depth relationships for cirrus and deep stratiform ice cloud layers, *J. Appl. Meteorol.*, *42*, 1369–1390, doi:10.1175/1520-0450(2003)042<1369:IWPDRF>2.0.CO;2.
- Hong, S.-Y., and J.-O. Lim (2006), The WRF single-moment 6-class microphysics scheme (WSM6), *J. Korean Meteorol. Soc.*, *42*, 129–151.
- Hong, S.-Y., Y. Noah, and J. Dudhia (2006), A new vertical diffusion package with an explicit treatment of entrainment processes, *Mon. Weather Rev.*, *134*, 2318–2341, doi:http://dx.doi.org/10.1175/MWR3199.1.
- Houtekamer, P. L., H. L. Mitchell, G. Pellerin, M. Buehner, M. Charron, L. Spacek, and B. Hansen (2005), Atmospheric data assimilation with an ensemble Kalman filter: Results with real observations, *Mon. Weather Rev.*, *133*, 604–620, doi:10.1175/MWR-2864.1.
- Iacono, M. J., J. S. Delamere, E. J. Mlawer, M. W. Shephard, S. A. Clough, and W. D. Collins (2008), Radiative forcing by long-lived greenhouse gases: Calculations with the AER radiative transfer models, *J. Geophys. Res.*, *113*, D13103, doi:10.1029/2008JD009944.
- Kain, J. S. (2004), The Kain-Fritsch convective parameterization: An update, *J. Appl. Meteorol.*, *43*, 170–181, doi:10.1175/1520-0450(2004)043<0170:TKCPAU>2.0.CO;2.
- Kain, J. S., and J. M. Fritsch (1993), Convective parameterization for mesoscale models: The Kain-Fritsch scheme, in *The Representation of Cumulus Convection in Numerical Models*, edited by K. A. Emanuel and D. J. Raymond, pp. 165–170, Am. Meteorol. Soc., Boston, Mass.
- Köpken, C., G. Kelly, and J.-N. Thepaut (2004), Assimilation of Meteosat radiance data within the 4D-Var system at ECMWF: Assimilation experiments and forecast impact, *Q. J. R. Meteorol. Soc.*, *130*, 2277–2292, doi:10.1256/qj.02.230.
- Krishnamurti, T. N., K. Ingles, S. Cocke, T. Kitade, and R. Pasch (1984), Details of low latitude medium range numerical weather prediction using a global spectral model, *J. Meteorol. Soc. Jpn.*, *62*, 613–649.
- Li, J., and H. Liu (2009), Improved hurricane track and intensity forecast using single field-of-view advanced IR sounding measurements, *Geophys. Res. Lett.*, *36*, L11813, doi:10.1029/2009GL038285.
- Liu, Y.-C., S.-H. Chen, and F.-C. Chien (2011), Impact of MODIS and AIRS total precipitable water on modifying the vertical shear and Hurricane Emily simulations, *J. Geophys. Res.*, *116*, D02126, doi:10.1029/2010JD014528.
- McBride, J. L., and R. M. Zehr (1981), Observational analysis of tropical cyclone formation. Part II: Comparison of non-developing versus developing systems, *J. Atmos. Sci.*, *38*, 1132–1151, doi:10.1175/1520-0469(1981)038<1132:OAOTCF>2.0.CO;2.
- Miloshevich, L. M., H. Vomel, D. N. Whiteman, B. M. Lesht, F. J. Schmidlin, and F. Russo (2006), Absolute accuracy of water vapor measurements from six operational radiosonde types launched during AWEX-G, and implications for AIRS validation, *J. Geophys. Res.*, *111*, D09S10, doi:10.1029/2005JD006083.
- Mitchell, H. L., P. L. Houtekamer, and G. Pellerin (2002), Ensemble size, balance, and model-error representation in an ensemble Kalman filter, *Mon. Weather Rev.*, *130*, 2791–2808, doi:10.1175/1520-0493(2002)130<2791:ESBAME>2.0.CO;2.
- Munro, R., C. Kopken, G. Kelly, J.-N. Thepaut, and R. Sanders (2004), Assimilation of Meteosat radiance data within the 4D-Var system at ECMWF: Data quality monitoring, bias correction, and single-cycle experiments, *Q. J. R. Meteorol. Soc.*, *130*, 2293–2313, doi:10.1256/qj.02.229.
- O'Dell, C. W., A. K. Heidinger, T. Greenwald, P. Bauer, and R. Bennartz (2006), The successive-order-of-interaction radiative transfer model. Part II: Model performance and applications, *J. Appl. Meteorol. Climatol.*, *45*, 1403–1413, doi:10.1175/JAM2409.1.
- Otkin, J. A. (2010), Clear and cloudy sky infrared brightness temperature assimilation using an ensemble Kalman filter, *J. Geophys. Res.*, *115*, D19207, doi:10.1029/2009JD013759.
- Otkin, J. A. (2012), Assessing the impact of the covariance localization radius when assimilating infrared brightness temperature observations using an ensemble Kalman filter, *Mon. Weather Rev.*, *140*, 543–561, doi:10.1175/MWR-D-11-00084.1.
- Otkin, J. A., and T. J. Greenwald (2008), Comparison of WRF model-simulated and MODIS-derived cloud data, *Mon. Weather Rev.*, *136*, 1957–1970, doi:10.1175/2007MWR2293.1.
- Otkin, J. A., T. J. Greenwald, J. Sieglaff, and H.-L. Huang (2009), Validation of a large-scale simulated brightness temperature dataset using SEVIRI satellite observations, *J. Appl. Meteorol. Climatol.*, *48*, 1613–1626, doi:10.1175/2009JAMC2142.1.
- Palmen, E. (1948), On the formation and structure of tropical cyclones, *Geophysics*, *3*, 26–38.
- Pu, A., and L. Zhang (2010), Validation of Atmospheric Infrared Sounder temperature and moisture profiles over tropical oceans and their impact on numerical simulations of tropical cyclones, *J. Geophys. Res.*, *115*, D24114, doi:10.1029/2010JD014258.
- Puri, K., and N. E. Davidson (1992), The use of infrared satellite cloud imagery data as proxy data for moisture and diabatic heating in data assimilation, *Mon. Weather Rev.*, *120*, 2329–2341, doi:10.1175/1520-0493(1992)120<2329:TUOISC>2.0.CO;2.
- Puri, K., and M. J. Miller (1990), The use of satellite data in the specification of convective heating for diabatic initialization and moisture adjustment in numerical weather prediction models, *Mon. Weather Rev.*, *118*, 67–93, doi:10.1175/1520-0493(1990)118<0067:TUOSDI>2.0.CO;2.
- Raymond, W. H., G. S. Wade, and T. H. Zapotocny (2004), Assimilating GOES brightness temperatures. Part I: Upper-tropospheric moisture, *J. Appl. Meteorol.*, *43*, 17–27, doi:10.1175/1520-0450(2004)043<0017:AGBTPI>2.0.CO;2.
- Riehl, H. (1948), On the formation of typhoons, *J. Meteorol.*, *5*, 247–265, doi:10.1175/1520-0469(1948)005<0247:OTFOT>2.0.CO;2.
- Sanders, F., and J. R. Gyakum (1980), Synoptic-dynamic climatology of the “bomb,” *Mon. Weather Rev.*, *108*, 1589–1606, doi:10.1175/1520-0493(1980)108<1589:SDCOT>2.0.CO;2.
- Schmit, T. J., W. F. Feltz, W. P. Menzel, J. Jung, A. P. Noel, J. N. Heil, J. P. Nelson, and G. S. Wade (2002), Validation and use of GOES sounder moisture information, *Weather Forecast.*, *17*, 139–154, doi:10.1175/1520-0434(2002)017<0139:VAUOGS>2.0.CO;2.
- Schmit, T. J., M. M. Gunshor, W. P. Menzel, J. J. Gurka, J. Li, and A. S. Bachmeier (2005), Introducing the next-generation Advanced Baseline Imager on GOES-R, *Bull. Am. Meteorol. Soc.*, *86*, 1079–1096, doi:10.1175/BAMS-86-8-1079.

- Seaman, C. J., M. Sengupta, and T. H. Vonder Haar (2010), Mesoscale satellite data assimilation: Impact of cloud-affected infrared observations on a cloud-free initial model state, *Tellus, Ser. A*, *62*, 298–318.
- Seemann, S. W., E. E. Borbas, R. O. Knuteson, G. R. Stephenson, and H.-L. Huang (2008), Development of a global infrared land surface emissivity database for application to clear sky sounding retrievals from multispectral satellite radiance measurements, *J. Appl. Meteorol. Climatol.*, *47*, 108–123, doi:10.1175/2007JAMC1590.1.
- Singh, R., P. K. Pal, C. M. Kishtawal, and P. C. Joshi (2008), Impact of Atmospheric Infrared Sounder data on the numerical simulation of a historical Mumbai rain event, *Weather Forecast.*, *23*, 891–913, doi:10.1175/2008WAF2007060.1.
- Singh, R., P. K. Pal, and P. C. Joshi (2010), Assimilation of Kalpana very high resolution radiometer water vapor channel radiances into a mesoscale model, *J. Geophys. Res.*, *115*, D18124, doi:10.1029/2010JD014027.
- Singh, R., C. M. Kishtawal, and P. K. Pal (2011), A comparison of the performance of Kalpana and HIRS water vapor radiances in the WRF 3D-Var assimilation system for mesoscale weather predictions, *J. Geophys. Res.*, *116*, D08113, doi:10.1029/2010JD014969.
- Skamarock, W. C., J. B. Klemp, J. Dudhia, D. O. Gill, D. M. Barker, W. Wang, and J. G. Powers (2005), A description of the Advanced Research WRF Version 2, *NCAR Tech. Note/TN-468+STR*, 88 pp., NCAR, Boulder, Colo.
- Stengel, M., M. Lindskog, P. Unden, N. Gustafsson, and R. Bennartz (2010), An extended observation operator in HIRLAM 4D-VAR for the assimilation of cloud-affected satellite radiances, *Q. J. R. Meteorol. Soc.*, *136*, 1064–1074, doi:10.1002/qj.621.
- Torn, R. D., G. J. Hakim, and C. Snyder (2006), Boundary conditions for limited-area ensemble Kalman filters, *Mon. Weather Rev.*, *134*, 2490–2502, doi:10.1175/MWR3187.1.
- Whitaker, J. S., and T. M. Hamill (2002), Ensemble data assimilation without perturbed observations, *Mon. Weather Rev.*, *130*, 1913–1924, doi:10.1175/1520-0493(2002)130<1913:EDAWPO>2.0.CO;2.
- Wu, X., G. R. Diak, C. M. Hayden, and J. A. Young (1995), Short-range precipitation forecasts using assimilation of simulated satellite water vapor profiles and column cloud liquid water amounts, *Mon. Weather Rev.*, *123*, 347–365, doi:10.1175/1520-0493(1995)123<0347:SRPFUA>2.0.CO;2.
- Zapotocny, T. H., W. P. Menzel, J. Jung, and J. P. Nelson (2005), A four-season impact study of rawinsonde, GOES, and POES data in the Eta Data Assimilation System. Part I: The total contribution, *Weather Forecast.*, *20*, 161–177, doi:10.1175/WAF837.1.